Embryological Evidence Identifies Wing Digits in Birds as Digits 1, 2, and 3

Koji Tamura, *et al.*

Science **331**, 753 (2011);
DOI: 10.1126/science.1198229

longitudinal arch in the Hadar foot (*35*, *37*). The morphology of the AL 333-160 Hadar fourth metatarsal eliminates that objection.

The 4.4-million-year-old skeleton of *Ardipithecus ramidus* suggests that the transition to terrestrial bipedality occurred in the earliest hominins, while selection maintained adaptations in the foot for arboreal climbing and grasping (*25*). By at least 3.2 million years ago, the fundamental attributes of human pedal anatomy and function were in place. This includes the transformation of the first toe and associated musculature from a grasping structure to one designed for propulsion and shock absorption [review in (*1*)]. Evidence from the Hadar fourth metatarsal adds to this human-like portrait of permanent longitudinal and transverse bony arches in the sole of the foot. The evolutionary trajectory suggested by these fossil remains makes it unlikely that selection continued to favor substantial arboreal behaviors by the time of *A. afarensis*.

References and Notes

1. L. Klenerman, B. Wood, *The Human Foot: A Companion to Clinical Studies* (Springer, London, 2006).
2. D. J. Morton, *Am. J. Phys. Anthropol.* **7**, 1 (1924).
3. R. F. Ker, M. B. Bennett, S. R. Bibby, R. C. Kester, R. M. Alexander, *Nature* **325**, 147 (1987).
4. R. M. Alexander, *J. Exp. Biol.* **160**, 55 (1991).
5. I. A. Kapandji, *The Physiology of the Joints, Volume 2: The Lower Limb* (E. & S. Livingstone, Edinburgh, 1985).
6. G. Sammarco, in *Basic Biomechanics of the Musculoskeletal System*, M. Nordin, V. Frankel, Eds. (Lippincott Williams and Wilkens, Philadelphia, 1989), pp. 163–182.
7. J. H. Hicks, *J. Anat.* **87**, 345 (1953).
8. H. Elftman, J. Manter, *Am. J. Phys. Anthropol.* **20**, 69 (1935).
9. D. L. Gebo, *Am. J. Phys. Anthropol.* **89**, 29 (1992).
10. J. DeSilva, *Am. J. Phys. Anthropol.* **141**, 1 (2009).
11. G. Berillon, *Hum. Evol.* **18**, 113 (2003).
12. E. Sarmiento, *Am. J. Phys. Anthropol.* **12** (suppl.), 157 (1991).
13. P. Lamy, *J. Hum. Evol.* **15**, 31 (1986).
14. J. T. Stern Jr., R. L. Susman, *Am. J. Phys. Anthropol.* **60**, 279 (1983).
15. W. E. H. Harcourt-Smith, thesis (University College London, 2002).
16. W. E. H. Harcourt-Smith, L. C. Aiello, *J. Anat.* **204**, 403 (2004).
17. R. C. Walter, *Geol. Soc. Am.* **22**, 6 (1994).
18. W. Kimbel, L. Delezene, *Yearb. Phys. Anthropol.* **140**, 2 (2009).
19. B. M. Latimer, C. O. Lovejoy, D. C. Johanson, Y. Coppens, *Am. J. Phys. Anthropol.* **57**, 701 (1982).
20. Y. Deloison, *Biometry Hum. Anthropol.* **21**, 189 (2003).
21. B. Zipfel, J. M. DeSilva, R. S. Kidd, *Am. J. Phys. Anthropol.* **140**, 532 (2009).
22. L. Aiello, C. Dean, *An Introduction to Human Evolutionary Anatomy* (Academic Press, London, 1990).
23. O. J. Lewis, *J. Anat.* **130**, 833 (1980).
24. H. Pontzer *et al.*, *J. Hum. Evol.* **58**, 492 (2010).
25. C. Lovejoy, B. Latimer, G. Suwa, B. Asfaw, T. White, *Science* **326**, 72 (2009).
26. K. D'Août, P. Aerts, D. De Clercq, K. De Meester, L. Van Elsacker, *Am. J. Phys. Anthropol.* **119**, 37 (2002).
27. B. Latimer, C. O. Lovejoy, *Am. J. Phys. Anthropol.* **83**, 13 (1990a).
28. E. E. Vereecke, P. Aerts, *J. Exp. Biol.* **211**, 3661 (2008).
29. E. Vereecke, K. D'Août, D. De Clercq, L. Van Elsacker, P. Aerts, *Am. J. Phys. Anthropol.* **120**, 373 (2003).
30. M. W. Hamrick, *J. Morphol.* **230**, 113 (1996).
31. M. H. Day, J. R. Napier, *Nature* **201**, 969 (1964).
32. D. N. Gomberg, B. Latimer, *Am. J. Phys. Anthropol.* **63**, 164 (1984).
33. T. D. White, G. Suwa, *Am. J. Phys. Anthropol.* **72**, 485 (1987).
34. R. Kidd, *Austral. Pod.* **27**, 35 (1993).
35. W. Harcourt-Smith, C. Hilton, *Am. J. Phys. Anthropol.* **40** (suppl.), 112 (2005).
36. M. R. Bennett *et al.*, *Science* **323**, 1197 (2009).
37. R. H. Tuttle, D. M. Webb, M. Baksh, *Hum. Evol.* **6**, 193 (1991).

38. The authors thank the members of the Hadar Research Project (1990–2004) and the Hadar Paleoanthropology Field School (2007 and 2009) for their dedication and hard work, and the directors and staff of the National Museum of Ethiopia, Cleveland Museum of Natural History, and National Museums of Kenya for facilitating the analytical research reported here. Fieldwork permissions were kindly granted by the Authority for Research and Conservation of Cultural Heritage, Ethiopian Ministry of Culture and Tourism, and the Culture and Tourism Bureau of the Afar Regional State government. We thank J. DeSilva, J. M. Plavcan, and G. Schwartz for helpful comments. The analytical research was supported by NSF (grants NSF SBR-9601025 and NSF BCS-0333296), the University of Missouri Research Board and University of Missouri Research Council, and the Institute of Human Origins at Arizona State University.

Supporting Online Material

www.sciencemag.org/cgi/content/full/331/6018/750/DC1
Tables S1 and S2

9 December 2010; accepted 12 January 2011
10.1126/science.1201463

Embryological Evidence Identifies Wing Digits in Birds as Digits 1, 2, and 3

Koji Tamura,*† Naoki Nomura,* Ryohei Seki, Sayuri Yonei-Tamura, Hitoshi Yokoyama

The identities of the digits of the avian forelimb are disputed. Whereas paleontological findings support the position that the digits correspond to digits one, two, and three, embryological evidence points to digit two, three, and four identities. By using transplantation and cell-labeling experiments, we found that the posteriormost digit in the wing does not correspond to digit four in the hindlimb; its progenitor segregates early from the zone of polarizing activity, placing it in the domain of digit three specification. We suggest that an avian-specific shift uncouples the digit anlagen from the molecular mechanisms that pattern them, resulting in the imposition of digit one, two, and three identities on the second, third, and fourth anlagens.

The morphology of the hand of tetrapods is derived from a five-fingered plan, the pentadactyl limb. In many tetrapods, some of the digits have been secondarily lost. Consequently, knowing which digits are present is a characteristic used to infer phylogenetic relationships between lineages. Close relationship between theropod dinosaurs and birds is evident, but the identities of avian hand digits remain controversial. Basal ornithischian dinosaurs, such as *Heterodontosaurs*, possessed a five-digit hand. In the process of theropod evolution, the posterior two digits (digits D4 and D5) (*1*) were lost, such that later theropods like the maniraptoran *Deinonychus* had only D1 to D3 (*2*–*4*). Given the known relationship between theropods and early birds, such as *Archaeopteryx*, paleontological evidence suggests that the digit identity of the avian wing is D1, D2, and D3. In contrast, embryological evidence based on condensation patterns of digits suggests that the modern bird wing comprises the D2, D3, and D4 of the pentadactyl ground state (*5*–*8*). In general, the fourth digit is the first visible digit (FVD) of tetrapod embryo development and is part of what has been termed the primary limb axis, which is aligned with the extension of the posterior zeugopod and the posterior basal autopod (*6*). In the chick embryo, the FVD occupies the posteriormost position in the three-digit chick forelimb but is still spatially aligned with the primary axis. Thus, the embryological view is that the FVD in the chick forelimb bud is designated as the fourth digit (*6*). To resolve the apparent disagreement between paleontological and embryological views, we investigated the early development of the posteriormost digit in the chick embryo (*9*).

Recent studies suggest that digit-specific developmental mechanisms determine digit identity. In the five-digit mouse limb bud, D4 and D5 and a posterior portion of D3 originate from descendants of *shh*-expressing zone of polarizing activity (ZPA) cells (*10*). Thus in the mouse, the FVD is derived from descendants of *shh*-expressing ZPA. In contrast, despite the ability of the ZPA of the chicken forelimb to induce all subsequent digits, it does not contribute to any digits when implanted into the host limb bud (Fig. 1, D and E) (*11*–*13*). This discrepancy may be attributable to the difference in digit numbers in mouse and chick limbs and thus provides an opportunity to further explore digit identity in the avian wing.

To examine the contribution of ZPA cells to subsequent digits on ectopic implantation, we performed a swapping transplantation of three-digit forelimb and four-digit hindlimb ZPAs in chick embryos (fig. S1) (*13*, *14*). We used chick embryos at stages 21/22 and 22 as donors for the ZPA grafts, because it is at these stages that autopod specification begins in both forelimb and hindlimb (*15*–*17*). Chick hindlimbs that received forelimb ZPA developed only hindlimb digits in a duplicated digit

Department of Developmental Biology and Neurosciences, Graduate School of Life Sciences, Tohoku University, Aobayama, Aoba-ku, Sendai 980-8578, Japan.

*These authors contributed equally to this work.
†To whom correspondence should be addressed. E-mail: tam@m.tohoku.ac.jp

pattern (Fig. 1A and fig. S7). Together with the result of chimera analysis (Fig. 1, D and E), these data indicate that chick forelimb ZPA induces all additional digits in the host. Implantation of hindlimb ZPA frequently gave rise to a hindlimb digit in the forelimb (Fig. 1B and fig. S7). Furthermore, this additional hindlimb digit was generated from donor cells (Fig. 1, F and G). These observations suggest that the posteriormost digit in the forelimb is induced by the ZPA at stages 21/22 and 22 and that the descendants of the hindlimb ZPA at these stages are capable of forming a digit. The transplant of an older hindlimb ZPA at stage 25, in which *shh* is expressed (*18*, *19*), produced no hindlimb digits, because digits primordial condensation of FVD is located outside the ZPA at this stage (*20*) (Fig. 1C and fig. S7).

Fate-mapping the ZPA provided further support for its differential contribution to digit cartilage in fore- and hindlimb. By using the vital dyes [lipophilic fluorescent dyes 1,1′-dioctadecyl-3,3,3′,3′-tetramethylindocarbocyanine perchlorate (DiI) and 3,3'-dioctadecyloxacarbocyanine perchlorate (DiO)], we found that a small mesenchymal area of the distal margin outside the forelimb ZPA at stage 22 contributed to the third digit in the wing (Fig. 2, A to C). Label inside the ZPA [within the *shh*-expression domain (fig. S1)] did not contribute to digit cartilage (Fig. 2, D to F and M). In the chick hindlimb bud at stage 22, label within the ZPA did contribute to the fourth digit (Fig. 2, J to L and N), whereas labeling mesenchymal cells neighboring the ZPA showed progeny distributed in the interdigital region between the third and fourth digits (Fig. 2, G to I). Heterospecific and homotopic implantation of the ZPA further confirmed the differential contributions of the ZPA to digit cartilage (fig. S2).

The above results suggest that by stage 22, when the digits are being specified, the progenitor of the posteriormost digit in the chick forelimb is located outside the ZPA, whereas that of the posteriormost hindlimb digit is inside the ZPA. Studies performed in the five-digit mouse have shown that the anteriormost digit is formed independently of the function of *shh* (*10*, *21*, *22*). It has also been suggested that specification of the second and third digits depends on the concentration of SHH protein diffusing from the ZPA and that the high levels of SHH protein found adjacent to the ZPA specify this digit progenitor as D3. Therefore, the FVD in the chick forelimb is D3. In contrast, in the hindlimb, we find that the FVD is formed by descendants of the ZPA at the stages, assigning this digit a D4 identity. Thus, the FVD in the three-digit chick forelimb is not homologous to the FVD in the four-digit hindlimb. When considered with the fact that the anteriormost digit, D1, is independent of *shh* function and shares molecular mechanisms in the mouse and chick that include the expression of certain genes (*Hoxd* and others) (*10*, *23*–*26*), a simple explanation is that the avian wing forms digits D1, D2, and D3, as in the ancestral theropods, whereas the avian leg forms digits D1, D2, D3, and D4, in correspondence with mouse digits D1, D2, D3, D4, and D5.

We next asked the location of digit progenitors before autopod specification by constructing a fate map of the posterior region of the stage 20 forelimbs and hindlimbs (Fig. 3 and fig. S3). Before their specification, forelimb D3 progenitor is found within the *shh*-expressing ZPA (Fig. 3B), whereas in the hindlimb, not D3 but D4 progenitor is found within the *shh*-expressing ZPA (Fig. 3, A and D, and fig. S3). Cell-labeling experiments further show that the forelimb D3 progenitor segregates from the *shh*-expressing domain between stage 20 and 22 but before specification (Fig. 3C and fig. S4). Thus, the forelimb D3 progenitor is located inside the ZPA at stage 20 but outside it at stage 22. This segregation allows the digit progenitor inside the early ZPA to access to the juxta-ZPA signals later that specify digit D3 identity. In contrast, such segregation does not occur in the hindlimb (Fig. 3F and fig. S4). This change inside the early forelimb ZPA accounts for what has been recognized as the "frame shift" that was thought to occur in the primordial condensation of the FVD in the chick forelimb (*2*). Although this change is not necessarily specific to the chick forelimb, because all progenitors eventually segregate from the ZPA (arrows in Fig. 4, bottom), what is unique to the chick wing is the heterochronic, premature separation of D3 progenitor from the avian forelimb ZPA, which causes a heterotopic frame shift of digit anlage. Importantly, this reveals a derived transformation along the avian stem. This idea is supported by our findings that the domain of overlap between the apical ectodermal ridge (AER) and the ZPA is correlated with digit numbers be-

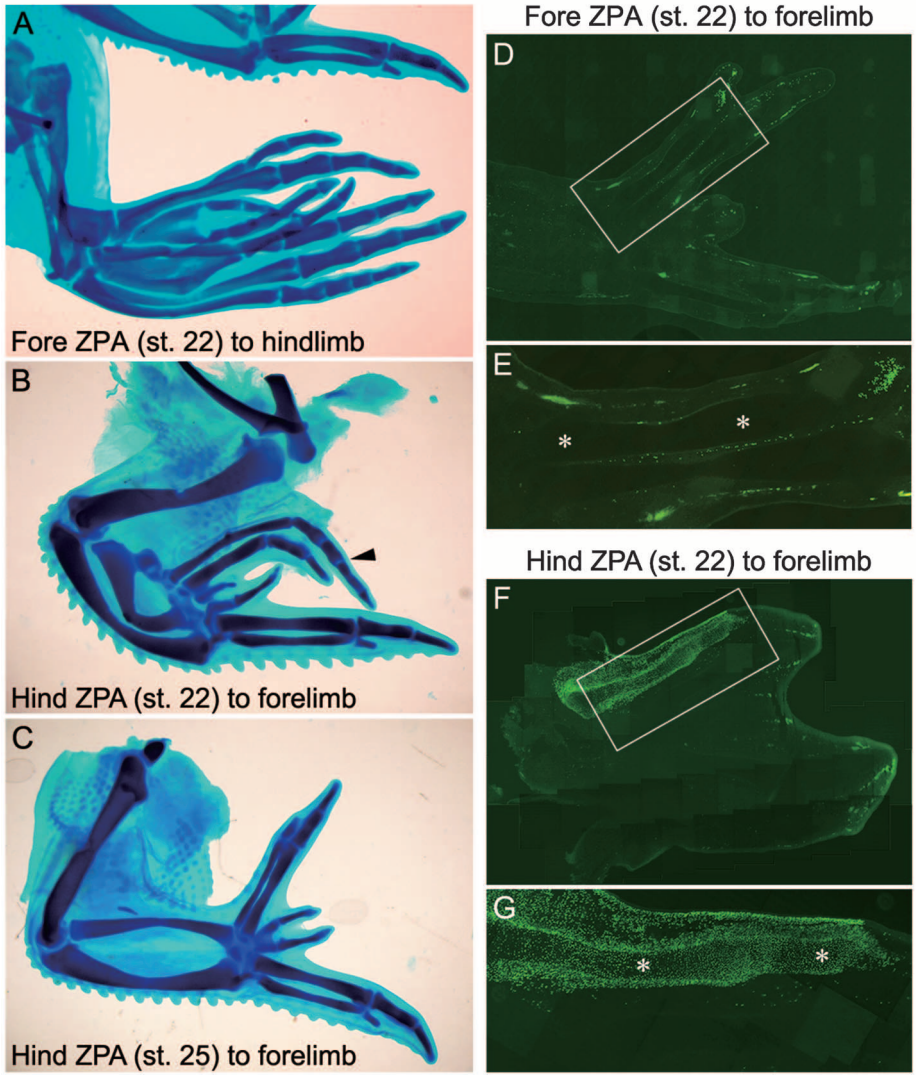

Fig. 1. Differential contributions of fore- and hindlimb ZPAs to duplicated digit cartilage. (**A**) Forelimb ZPA at stage 22 implanted into the hindlimb bud formed no forelimb digits. (**B**) After implantation of stage 22 hindlimb ZPA into the forelimb bud, the anteriormost digit (arrowhead) in the duplication showed hindlimb digit identity. (**C**) No hindlimb digit was produced by hindlimb ZPA at stage 25. (**D** to **G**) Distribution of ZPA cells in the duplicated forelimb. The boxes in (D) and (F) are magnified to show that the implanted stage-22 forelimb ZPA contributed little to cartilage formation [asterisks in (E)], whereas the anteriormost digit in the duplication was mainly composed of implanted stage-22 hindlimb ZPA-originating cells [asterisks in (G)].

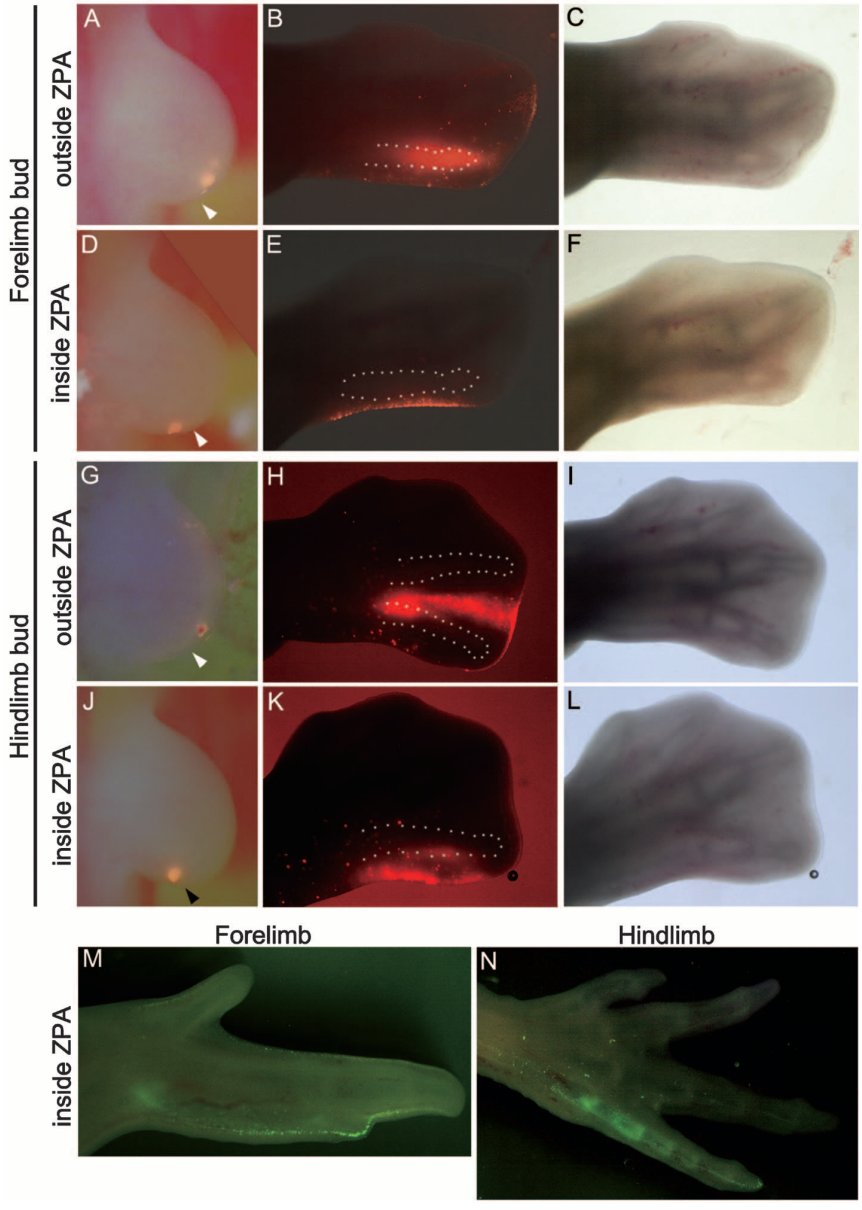

Fig. 2. DiI or DiO labeling of cells outside and inside the ZPA at stage 22. (**A** to **C**) Labeled cells outside the forelimb ZPA [estimated by the posterior edge of the AER, arrowhead in (A)] contributed to cartilage of the posteriormost digit ($n = 9$). (**D** to **F**, and **M**) Labeled cells inside the forelimb ZPA were not distributed to the posteriormost digit cartilage but were observed in the periphery of the autopod ($n = 11$). (**G** to **L**, and **N**) Labeled cells outside the hindlimb ZPA were distributed to the interdigital region between D3 and D4 [(H) and (I), $n = 10$], and cells inside the hindlimb ZPA contributed to the formation of D4 [(K), (L), and (N), $n = 8$]. White dots [(B), (E), (H), and (K)] outline cartilage of D3 and D4 [(C), (F), (I), and (L)].

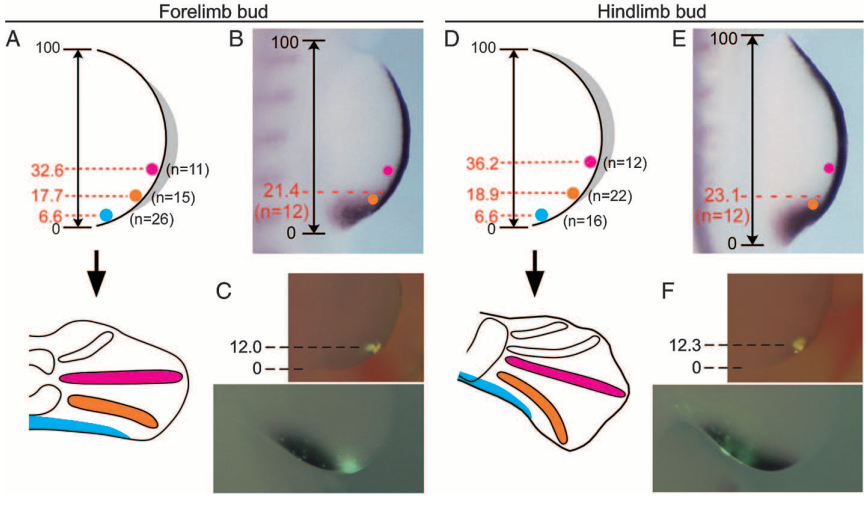

Fig. 3. Fate mapping at stage 20. (**A**) In the stage-20 forelimb bud, the average positions for the second- and third-digit progenitors and the posterior periphery were at 32.6%, 17.7%, and 6.6% of the anterior-posterior (AP) axis [100% (anterior end) to 0% (posterior end)], respectively. (**D**) In the stage-20 hindlimb bud, the average positions for the third- and fourth-digit progenitors and the posterior periphery were at 36.2%, 18.9%, and 6.6% of the AP axis, respectively. *Shh* expression in the stage-20 limb bud showed the anterior edge of the expression domain at 21.4% (forelimb bud) (**B**) and 23.1% (hindlimb bud) (**E**). The average position for the posteriormost digit in both the forelimb bud [17.7% in (A)] and hindlimb bud [18.9% in (B)] was inside the anterior edge of the *shh* expression domain. (**C** and **F**) DiO-labeled cells at 12.0% (the third-digit progenitor inside the ZPA) of the stage-20 forelimb bud were located outside the ZPA after 18 hours (C), whereas DiO-labeled hindlimb cells at 12.3% (the fourth-digit progenitor inside the ZPA) remained inside the ZPA after 18 hours (F). Detailed data are also shown in figs. S3 and S4.

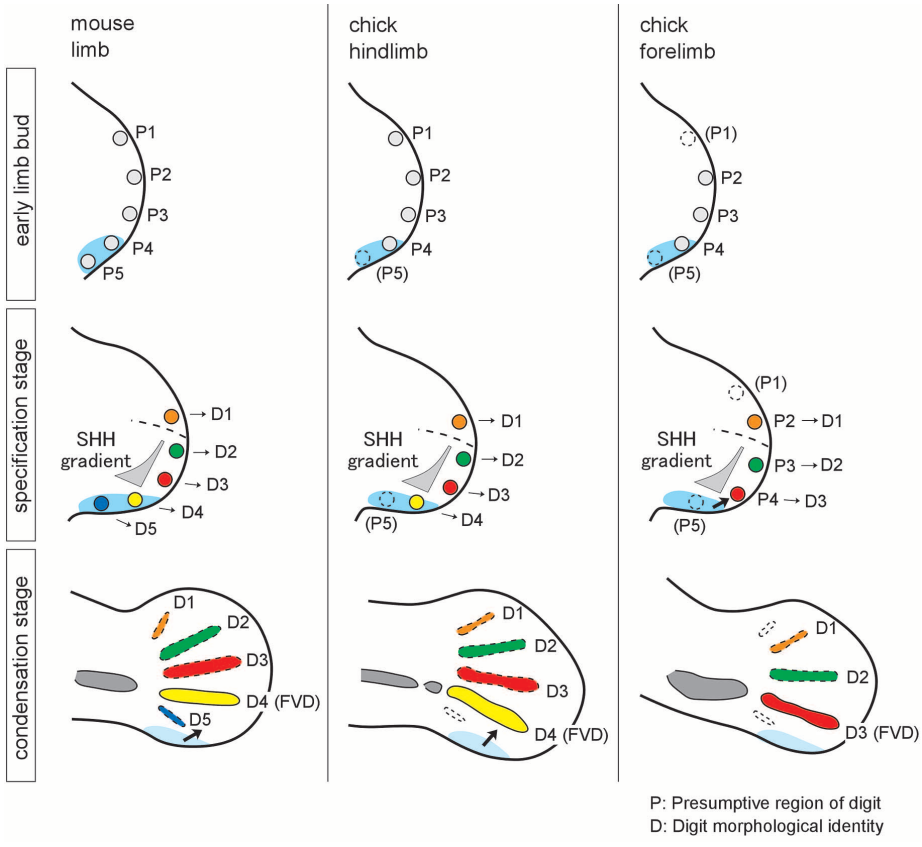

Fig. 4. Digit development. (**Top**) At early limb bud stage, there are five modules (indicated by gray circles and P) that act as digit progenitors. P4 and P5 are located inside the ZPA (light blue). Dotted circle indicates a module that does not result in a digit. (**Middle**) At the digit-specification stage, a distinct molecular mechanism (indicated by colors) confers digit morphological identity (D) to each module. In the chick forelimb, P4, which has been separated from the ZPA by the frame shift (arrow), is specified as D3. (**Bottom**) By the condensation stage, all digit primordia separate from the ZPA (arrows), and the FVD cartilage differentiates while simultaneously receiving local information from the interdigital region (*31*).

tween species (fig. S5) and is reduced early in the chick forelimb bud.

The posteriormost digit primordium, which condenses to give rise to the FVD cartilage at the later stages (Fig. 4, bottom), has already been specified for digit identity (in Fig. 4, middle). Thus, among tetrapods, even when the FVD is on the primary axis, it need not show correspondence of digit identity. Indeed, we show that in the hindlimb it is the second digit condensation that has been reallocated to the primary axis in the absence of progenitors for the posterior two digits (fig. S6). Cohn *et al*. further showed that proximal limb elements are not required for digit development and suggested that the digits are not sequential to the branching and segmentation of the precartilaginous proximal elements of the limb (*27*). Moreover, recent findings show that the order of digit condensation in the mouse does not necessarily correlate with digit identity (*28*). These arguments allow us to conclude that the concept of FVD on the primary axis is not developmentally coupled with a particular digit identity. Furthermore, the primary axis-digit D4 hypothesis is not supported in birds, enabling us to reconcile embryonic patterns with paleontological data.

Through analysis of the developmental processes that precede condensation, we have identified the posteriormost digit in the chick forelimb as D3, corresponding to the third digit in the mouse. Like the mouse, it is specified by SHH protein signaling outside the ZPA (Fig. 4). However, before digit specification, this posteriormost-digit progenitor in the chick forelimb bud, like that in the hindlimb, is found in the region of the fourth anlage (P4) (Fig. 4, top) on the basis of the pentadactyl ground state for the chick limb (*8*, *29*). In the forelimb, P4 rapidly separates from the ZPA, and this shift imposes the digit D3 identity onto P4 during the specification of the autopod (Fig. 4, middle). This supports a model in which the developmental mechanism for digit specification is not only evolutionarily but also developmentally uncoupled from the positional identities (P1 to P5) within the pentadactyl ground state. This uncoupling allows the mechanism of morphological specification to shift along the digit progenitors and as a result acquire a shifted developmental code, as compared with the ancestral pattern, through this ontogenetic frame shift as seen in axial morphology (*30*). The frame shift can be viewed as a secondary event that takes place early in the forelimb bud development, and, in this sense, the chick forelimb bud before the shift can be viewed as its ancestral state (Fig. 4, top). Thereafter, P4 of the avian wing comes to lie outside the domain of ZPA and is now brought into a developmental trajectory of shifted morphological identity, as an apomorphic feature of avian morphogenesis. We conclude that the avian wing has digits one, two, and three from the developmental view point, as did the forelimbs of ancestral dinosaur, and the developmental shift in chick wing bud mirrors the sequence of evolutionary changes in forelimb morphologies of theropods.

References and Notes

1. Digit morphological identity (distinguishing a thumb from an index finger by anatomical features) is designated as D1 to D5 in this study.
2. G. P. Wagner, J. A. Gauthier, *Proc. Natl. Acad. Sci. U.S.A.* **96**, 5111 (1999).
3. Z. Zhou, *Naturwissenschaften* **91**, 455 (2004).
4. A. O. Vargas, J. F. Fallon, *J. Exp. Zool.* **304B**, 206 (2005).
5. J. R. Hinchliffe, in *Vertebrate Limb and Somite Morphogenesis*, D. A. Ede, J. R. Hinchliffe, M. Balls, Eds. (Cambridge Univ. Press, Cambridge, 1977), pp. 293–309.
6. A. C. Burke, A. Feduccia, *Science* **278**, 666 (1997).
7. F. Galis, M. Kundrat, J. A. J. Metz, *J. Exp. Zool.* **304B**, 198 (2005).
8. H. C. Larsson, G. P. Wagner, *J. Exp. Zool.* **294**, 146 (2002).
9. Materials and methods are available as supporting material on *Science* Online.
10. B. D. Harfe *et al*., *Cell* **118**, 517 (2004).
11. L. Wolpert, *Principles of Development* (Oxford Univ. Press, Oxford, ed. 3, 2007).
12. D. J. Wilson, J. R. Hinchliffe, *Development* **99**, 99 (1987).
13. J. R. Hinchliffe, A. Sansom, *J. Embryol. Exp. Morphol.* **86**, 169 (1985).
14. D. Summerbell, C. Tickle, in *Vertebrate Limb and Somite Morphogenesis*, D. A. Ede, J. R. Hinchliffe, M. Balls, Eds. (Cambridge Univ. Press, Cambridge, 1977), pp. 41–53.
15. D. Summerbell, J. H. Lewis, *J. Embryol. Exp. Morphol.* **33**, 621 (1975).
16. K. Sato, Y. Koizumi, M. Takahashi, A. Kuroiwa, K. Tamura, *Development* **134**, 1397 (2007).
17. D. A. Rowe, J. F. Fallon, *J. Embryol. Exp. Morphol.* **68**, 1 (1982).
18. R. D. Riddle, R. L. Johnson, E. Laufer, C. Tabin, *Cell* **75**, 1401 (1993).
19. L. S. Honig, D. Summerbell, *J. Embryol. Exp. Morphol.* **87**, 163 (1985).
20. M. C. M. Welten, F. J. Verbeek, A. H. Meijer, M. K. Richardson, *Evol. Dev.* **7**, 18 (2005).

21. P. J. Scherz, E. McGlinn, S. Nissim, C. J. Tabin, *Dev. Biol.* **308**, 343 (2007).
22. R. Zeller, J. López-Ríos, A. Zuniga, *Nat. Rev. Genet.* **10**, 845 (2009).
23. A. O. Vargas, T. Kohlsdorf, J. F. Fallon, J. Vandenbrooks, G. P. Wagner, *PLoS One* **3**, e3325 (2008).
24. A. Uejima *et al.*, *Dev. Growth Differ.* **52**, 223 (2010).
25. C. Chiang *et al.*, *Dev. Biol.* **236**, 421 (2001).
26. T. Amano, K. Tamura, *Dev. Dyn.* **233**, 326 (2005).
27. M. J. Cohn, C. O. Lovejoy, L. Wolpert, M. I. Coates, *Bioessays* **24**, 460 (2002).
28. J. Zhu *et al.*, *Dev. Cell* **14**, 624 (2008).
29. H. C. Larsson, A. C. Heppleston, R. M. Elsey, *J. Exp. Zool.* **314B**, 571 (2010).
30. A. C. Burke, C. E. Nelson, B. A. Morgan, C. Tabin, *Development* **121**, 333 (1995).
31. T. Suzuki, S. M. Hasso, J. F. Fallon, *Proc. Natl. Acad. Sci. U.S.A.* **105**, 4185 (2008).
32. We thank S. Kuratani for valuable discussions and comments on this study; R. Ladher, J. Fallon, H. Yajima, T. Suzuki, and D. Sipp for critical reading of this manuscript; and Y. Wakamatsu for supplying quail eggs. H.Y. was supported by Grant-in-Aid for Scientific Research on Innovative Areas. This work was supported by the Global Center of Excellence Program (J03) and grants from Japan Society for the Promotion of Science; the Ministry of Education, Culture, Sports, Science, and Technology of Japan; and the Toray Science Foundation.

Supporting Online Material

www.sciencemag.org/cgi/content/full/331/6018/753/DC1
Materials and Methods
Figs. S1 to S7
References

24 September 2010; accepted 12 January 2011
10.1126/science.1198229

Structure of MyTH4-FERM Domains in Myosin VIIa Tail Bound to Cargo

Lin Wu,* Lifeng Pan,* Zhiyi Wei, Mingjie Zhang†

The unconventional myosin VIIa (MYO7A) is one of the five proteins that form a network of complexes involved in formation of stereocilia. Defects in these proteins cause syndromic deaf-blindness in humans [Usher syndrome I (USH1)]. Many disease-causing mutations occur in myosin tail homology 4–protein 4.1, ezrin, radixin, moesin (MyTH4-FERM) domains in the myosin tail that binds to another USH1 protein, Sans. We report the crystal structure of MYO7A MyTH4-FERM domains in complex with the central domain (CEN) of Sans at 2.8 angstrom resolution. The MyTH4 and FERM domains form an integral structural and functional supramodule binding to two highly conserved segments (CEN1 and 2) of Sans. The MyTH4-FERM/CEN complex structure provides mechanistic explanations for known deafness-causing mutations in MYO7A MyTH4-FERM. The structure will also facilitate mechanistic and functional studies of MyTH4-FERM domains in other myosins.

Mutations in *Myo7a* (also known as *USH1B*), which encodes the unconventional myosin VIIa (MYO7A), cause both syndromic [Usher syndrome I (USH1)] and nonsyndromic (DFNB2 and DFNA11) deafness in humans (*1*, *2*). Although five genes have been associated with USH1 (*3*–*5*), mutations of *Myo7a* account for ~40 to 50% of all USH1 cases (*2*, *6*). In vitro studies have shown that the five USH1 proteins (MYO7A, harmonin, cadherin 23, protocadherin 15, and Sans) can form an integrated network of complexes (*4*, *7*–*9*). Mice containing mutations of any one of the USH1 proteins share common morphological defects in the stereocilia of hair cells (*10*, *11*).

The MYO7A tail contains a pair of myosin tail homology 4–protein 4.1, ezrin, radixin, moesin (MyTH4-FERM) tandems separated by a SH3 domain (a MyTH4-FERM tandem is defined as a MyTH4 domain and a FERM domain arranged right next to each other) (Fig. 1A). Two other unconventional myosins, myosin X and XV, also contain MyTH4-FERM tandem(s) in their tails and play critical roles in the formation of filopodia/stereocilia-like structures as well (*10*, *12*–*15*). More than 40 missense and 26 deletion/truncation disease-causing mutations are found in the two MYO7A MyTH4-FERM tandems (fig. S1). However, it is not clear why these mutations lead to disease phenotypes, though a recent study has shown that a truncation mutation in the second MyTH4-FERM tandem of MYO7A decreases the stability of the motor (*16*).

To elucidate MYO7A-mediated USH1 complex formation, we characterized the interaction between the first MYO7A MyTH4-FERM tandem and Sans, a scaffold protein known to bind to MYO7A (*7*, *17*, *18*). Analytical ultracentrifugation shows that the MyTH4-FERM-SH3 region of MYO7A (residues 965 to 1649, referred to as "MFS") is a stable monomer in solution (Fig. 1C). We confirmed the previous finding by Adato *et al.* (*7*) that the glutathione *S*-transferase (GST)–fused central domain of Sans [residues 295 to 390, referred to as "CEN" (fig. S2A)] strongly binds to MYO7A-MFS (Fig. 1B). Analytical ultracentrifugation also shows that untagged MYO7A-MFS and Sans CEN form a 1:1 stoichiometric complex in solution (Fig. 1C). We determined the stability of the complex by isothermal titration calorimetry, which gave a dissociation constant (K_d) ~ 50 nM (fig. S2B). Further extension of Sans to the C-terminal end does not change its MYO7A binding affinity (fig. S2D), indicating that Sans CEN encompasses the complete MYO7A binding region.

Nuclear magnetic resonance (NMR) spectra show that the isolated CEN is monomeric and unstructured in solution (fig. S2, E and F). CEN contains highly conserved stretches of residues at each end, separated by a variable connection sequence (fig. S2A). The binding affinities of the two fragments for MYO7A-MFS were $K_d \sim 2$ μM for CEN1 (residues 295 to 369) and ~270 μM for CEN2 (residues 369 to 390) (fig. S2D). Thus, both CEN1 and CEN2 interact directly with MFS, though CEN1 contributes to most of the binding energy. Both CEN1 and CEN2 are required for the colocalization of MYO7A-MFS and Sans in heterologous cells (fig. S3).

To gain further insight into the MYO7A/Sans interaction, we determined the crystal structure of the MFS/CEN complex at 2.8 Å resolution using a MYO7A isoform containing a 30-residue deletion in its MyTH4 domain (fig. S4 and table S1). This MYO7A-MFS isoform binds to Sans CEN with an affinity indistinguishable from that of MFS containing the 30-residue fragment (fig. S2C). The MYO7A-MFS adopts an overall Y-shaped architecture made up of three domains: (i) the N-terminal MyTH4 domain, (ii) the middle FERM domain, and (iii) the C-terminal SH3 domain (Fig. 1, D and E). The MyTH4 domain directly packs with the FERM F1 lobe, covering ~928 $Å^2$ in surface area. The interface is formed by conserved residues that are predominantly polar or charged (fig. S5, A and B).

As expected from its sequence similarity with FERM domains of known structures (*19*), MYO7A FERM is composed of F1, F2, and F3 lobes, which together form a cloverleaf configuration (Fig. 1D). The SH3 domain is coupled to the F3 lobe by a short α helix (fig. S5C). This hydrophobic α helix packs with the βB/βA/βE sheet of the SH3 domain and leaves SH3's canonical target-recognition pocket open (fig. S5D).

Surprisingly, we could only trace the Sans CEN1 region (residues 305 to 320) in the final complex structure model (Fig. 2A and fig. S6A), though SDS–polyacrylamide gel electrophoresis analysis confirmed the integrity of both MFS and CEN in the complex crystals (fig. S7). The defined CEN1 in the MFS/CEN complex contains 16 conserved residues (Fig. 2). The N-terminal half of CEN1 (residues 305 to 315) adopts a short β hairpin, and the C-terminal half (316 to 320) forms an extended structure (fig. S6B). CEN1 occupies all three interfaces formed between F1, F2, and F3 of the FERM domain and buries a surface area of ~958 $Å^2$. The first β strand of the CEN1 hairpin interacts with residues in the F2/F3 interface, the second β strand of the hairpin contacts the residues in the F1/F2 interface, and the last part of CEN1 fills in the F1/F3 gap (Fig. 2). The MFS/CEN1 interaction is different from known recognition modes of FERM domains (fig. S8). The interaction between CEN1 and FERM is mediated by extensive hydrophobic contacts, charge-charge interactions, and hydrogen bonding (Fig. 2B and fig. S9). Supporting the above structural data, the replacement of the conserved $Phe^{307}{}_{CEN1}$ or $Phe^{317}{}_{CEN1}$ with Glu or the substitution of $Phe^{1473}{}_{FERM}$ with

Division of Life Science, Molecular Neuroscience Center, State Key Laboratory of Molecular Neuroscience, Hong Kong University of Science and Technology, Clear Water Bay, Kowloon, Hong Kong.

*These authors contributed equally to this work.
†To whom correspondence should be addressed. E-mail: mzhang@ust.hk